

Optical-Microwave Scintillometer Evaporation measurements over a Saline Lake in a Heterogeneous Setting in the Atacama Desert

Journal of Hydrometeorology

Lobos-Roco, Felipe; Hartogensis, Oscar; Arellano, Jordi Vilà Guerau; Aguirre, Francisca; La Fuente, Alberto et al

<https://doi.org/10.1175/JHM-D-21-0100.1>

This publication is made publicly available in the institutional repository of Wageningen University and Research, under the terms of article 25fa of the Dutch Copyright Act, also known as the Amendment Taverne. This has been done with explicit consent by the author.

Article 25fa states that the author of a short scientific work funded either wholly or partially by Dutch public funds is entitled to make that work publicly available for no consideration following a reasonable period of time after the work was first published, provided that clear reference is made to the source of the first publication of the work.

This publication is distributed under The Association of Universities in the Netherlands (VSNU) 'Article 25fa implementation' project. In this project research outputs of researchers employed by Dutch Universities that comply with the legal requirements of Article 25fa of the Dutch Copyright Act are distributed online and free of cost or other barriers in institutional repositories. Research outputs are distributed six months after their first online publication in the original published version and with proper attribution to the source of the original publication.

You are permitted to download and use the publication for personal purposes. All rights remain with the author(s) and / or copyright owner(s) of this work. Any use of the publication or parts of it other than authorised under article 25fa of the Dutch Copyright act is prohibited. Wageningen University & Research and the author(s) of this publication shall not be held responsible or liable for any damages resulting from your (re)use of this publication.

For questions regarding the public availability of this publication please contact openscience.library@wur.nl

Optical Microwave Scintillometer Evaporation Measurements over a Saline Lake in a Heterogeneous Setting in the Atacama Desert

FELIPE LOBOS-ROCO,^a OSCAR HARTOGENSIS,^a JORDI VILÀ-GUERAU DE ARELLANO,^a FRANCISCA AGUIRRE,^b ALBERTO DE LA FUENTE,^c AND FRANCISCO SUÁREZ^{b,d,e}

^a *Meteorology and Air Quality, Wageningen University, Wageningen, Netherlands*

^b *Departamento de Ingeniería Hidráulica y Ambiental, Pontificia Universidad Católica de Chile, Santiago, Chile*

^c *Departamento de Ingeniería Civil, Universidad de Chile, Santiago, Chile*

^d *Centro de Desarrollo Urbano Sustentable, Santiago, Chile*

^e *Centro de Excelencia en Geotermia de los Andes, Santiago, Chile*

(Manuscript received 22 May 2021, in final form 4 April 2022)

ABSTRACT: Estimating lake evaporation is a challenge due to both practical considerations and theoretical assumptions embedded in indirect methods. For the first time, we evaluated measurements from an optical microwave scintillometer (OMS) system over an open-water body under arid conditions. The OMS is a line-of-sight remote sensing technique that can be used to measure the sensible and latent heat fluxes over horizontal areas with pathlengths ranging from 0.5 to 10 km. We installed an OMS at a saline lake surrounded by a wet-salt crust in the Salar del Huasco, a heterogeneous desert landscape in the Atacama Desert. As a reference, we used eddy covariance systems installed over the two main surfaces in the OMS footprint. We performed a footprint analysis to reconstruct the surface contribution to the OMS measured fluxes (80% water and 20% wet salt). Furthermore, we investigated the applicability of the Monin–Obukhov similarity theory (MOST), which was needed to infer fluxes from the OMS-derived structure parameters to the fluxes. The OMS structure parameters and MOST were compromised, which we mitigated by fitting MOST coefficients to the site conditions. We argue that the MOST deviation from values found in the literature is due to the effects of the surface heterogeneity and the nonlocal processes induced by regional circulation. With the available dataset we were not able to rule out instrument issues, such as additional fluctuations to the scintillation signal due to absorption or the effect of vibration in high-wind conditions. The adjusted MOST coefficients lowered by a factor of 1.64 compared to using standard MOST coefficients. For H and L_vE , we obtained zero-intercept linear regressions with correlations, R^2 , of 0.92 and 0.96, respectively. We conclude that advances in MOST are needed to successfully apply the OMS method in landscapes characterized by complex heterogeneity such as the Salar del Huasco.

KEYWORDS: Evaporation; Surface fluxes; Microwave observations; Measurements; Field experiments; Desert meteorology; Boundary layer

1. Introduction

In deserts, water is confined to specific areas such as saline lakes, rivers, wetlands, and salt flats, all of which act as highly localized evaporative pathways (Rosen 1994). For example, the mountain regions of the Atacama Desert (Altiplano) are formed by consecutive endorheic basins. These basins catch precipitation, which then enters the hydrological system. From this system, the water wells up at specific sites and produces relatively small shallow lakes surrounded by extended salt flats (Uribe et al. 2015). In this water-limited environment, evaporation is highly relevant since it represents the principal cause of water loss in the basins.

In arid regions, measuring evaporation over small saline lakes is particularly complicated for three main reasons. First is the surface heterogeneity, with strong contrasting surface fluxes (Suarez et al. 2020), requiring the necessity of a footprint analysis to interpret the measured evaporation. Second, the atmospheric boundary layer dynamics and their influence on the surface fluxes are affected by nonlocal effects such as

entrainment and advection of heat, moisture, and momentum (Lobos-Roco et al. 2021). Last, measuring evaporation over open waters always represents a challenge since installing instruments in water is technically challenging (Tanny et al. 2008; Nordbo et al. 2011).

To estimate evaporation, various direct and indirect methods with different theoretical assumptions and footprints were used and depend on the spatial scale of the subject under investigation (Abteu and Melesse 2012; Shuttleworth 2008). Within this context, we evaluated the applicability of an optical microwave scintillometer (OMS) to estimate open-water evaporation in arid regions. A scintillometer consists of a transmitter and a receiver. The transmitter emits a light beam toward the receiver, which measures the intensity of the fluctuations (the scintillation effect) caused by the turbulent transport of sensible heat and moisture crossing the instrument's path. The OMS combines two scintillometers with different wavelengths: the large aperture scintillometer (LAS) operates an optical light beam, while the microwave scintillometer (MWS) operates a microwave beam (Green et al. 2001; Kohsiek and Herben 1983). The optical beam is primarily sensitive to temperature fluctuations induced by the sensible heat flux, whereas the microwave beam is sensitive to both heat and water vapor (Hill et al. 1980). Note that Han et al. (2019) estimated lake

Corresponding author: Felipe Lobos-Roco, felipe.lobosroco@wur.nl, felipe.lobos.roco@gmail.com

evaporation using a LAS, which by itself yields only the sensible heat flux, which tend to be small over water. The technique used depends on an energy balance approach where the quality of the evaporation estimate depends on the net radiation measurements and hard to determine water storage flux.

The OMS presents several advantages related to its large footprint (10–100 km²) and its capacity to integrate heterogeneous landscapes (Lagouarde et al. 2002; Beyrich et al. 2012; Isabelle et al. 2020; Zhang et al. 2021; Meijninger et al. 2006; Evans et al. 2012; Ward et al. 2015). The OMS is specifically convenient for measuring evaporation over open water since the transmitter and receiver can be installed on opposite shores, concentrating the central part of the instrument's footprint over the water body. However, the OMS method also presents disadvantages in the flux calculation due to its dependency on the Monin–Obukhov similarity theory (MOST; Monin and Obukhov (1954)) and its underlying assumptions, such as horizontal homogeneity and the absence of outer scale processes. MOST connects turbulence-related quantities to turbulent fluxes through standard formulations determined empirically in field experiments and assumed to be universally applicable. This assumption is questionable when nonlocal contributions to the exchange process intervene (Kooijmans and Hartogensis 2016; Li et al. 2012).

The Altiplano of the Atacama Desert region presents interesting conditions to evaluate the strengths and weaknesses of the OMS method. We performed a 10-day field experiment called E-DATA, which was aimed at understanding the processes that control the evaporation of the saline lake in the Salar del Huasco in the Altiplano of the Atacama Desert (Suarez et al. 2020; Lobos-Roco et al. 2021). Part of the E-DATA experiment included the critical evaluation of the OMS method to determine open-water evaporation in a heterogeneous setting. To this end, we installed an OMS over the saline lake along with a small network of three eddy covariance (EC) systems, including one in the water body, covering the heterogeneous surfaces in the Salar del Huasco to serve as a reference.

Within this framework, we addressed the following research question: how accurate are the evaporation measurements performed by an OMS over an open-water body under arid and windy atmospheric conditions? To answer this question, we integrated into our analysis 1) the dynamic surface and atmospheric boundary layer conditions and 2) the evaluation of the MOST functions used to derive the surface fluxes and the impacts of both footprints and MOST function on the measurement of surface fluxes.

2. Methodology

This section begins with an overview of the measurement principles of the OMS and the EC systems, followed by descriptions of the calculation steps required to obtain surface fluxes from the OMS and EC measurements. Last, we describe the model used for calculating the OMS and EC footprints.

a. OMS versus EC method

Figure 1 provides an overview of some key aspects of the OMS and EC methods. Figure 1a summarizes the processing chain of the OMS to obtain surface fluxes from the OMS light intensity fluctuations, expressed as the variance of logarithm of the intensity fluctuations, $\sigma_{\ln(I)}^2$. The OMS beams experience fluctuations in the intensity of the light due to the eddies that cross them. The statistic that captures the intensity of these fluctuations, $\sigma_{\ln(I)}^2$, is related to the structure parameter of the refractive index C_n^2 (step I in Fig. 1a), which is a spatial statistic that quantifies the turbulence intensity. The turbulent eddies that mainly contribute to the scintillation effect are of one typical size, i.e., the aperture diameter, D ($= 0.15$ m) for the LAS and the Fresnel length scale, $F = \sqrt{\lambda L}$, for the MWS, where λ ($= 1.8$ mm) is the wavelength and L is the scintillometer pathlength ($0.5 < L < 10$ km). Typical values for F are 1–3 m. These eddy sizes typically correspond to the spectral inertial subrange (Kolmogorov 1941). The LAS is mainly sensitive to temperature fluctuations, whereas the MWS is sensitive to both temperature and humidity fluctuations brought about by the transport of turbulent eddies. Combining the measurements from both scintillometers allows to solve the temperature and humidity fluctuations in terms of the structure parameters of temperature and humidity, C_T^2 and C_q^2 (step II in Fig. 1a). These structure parameters, along with additional measurements of wind speed U and an estimate of the roughness length z_0 , are related to the fluxes of H and $L_v E$ following MOST formulations (step III in Fig. 1a). In section 2b and 2c, we make the processing steps more explicit.

Figure 1b highlights the main differences of the EC method in determining surface fluxes with respect to the OMS method: fluxes are calculated directly (i.e., do not rely on MOST) from the time series of high-frequency measurements of the 3D wind vector fluctuations (u' , v' , w'), as well as fluctuations of air temperature (T') and water vapor (q') as the covariance of the vertical wind speed, w , and T for the sensible heat flux ($H \sim w'T'$), with for the latent flux ($L_v E \sim w'q'$) and with for the momentum flux ($\tau \sim w'u'$). In contrast to the scintillometer that only considers a limited range of inertial-range eddy sizes around one dominant eddy scale in the flux estimate (e.g., Tatarski 1961; Wang et al. 1978), the EC method integrates all eddy sizes that contribute to the flux transport. The EC footprint, i.e., the source area of the turbulent eddies measured, is typically smaller than the scintillometer as it samples turbulent eddies at one point rather than over a path.

b. OMS fluxes

In the following section, we will explain the three processing steps of the OMS outlined in Fig. 1a. The first processing step relates the raw scintillation statistic $\sigma_{\ln(I)}^2$ (—) to C_n^2 (m^{-2/3}) for the optical and microwave scintillometer (step I in Fig. 1a). This relationship, which assumes that the OMS is only sensitive to eddies in the inertial subrange, is expressed through wave propagation theory in a turbulent medium (Tatarski 1961) from which it follows that

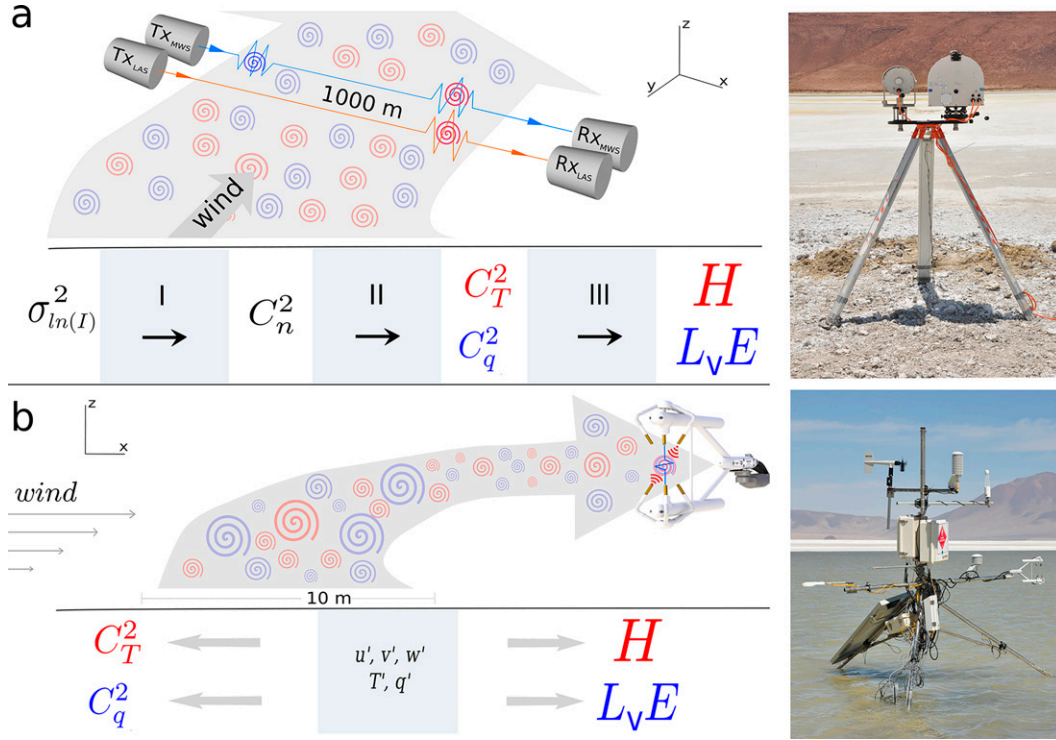


FIG. 1. Flowchart of the steps used to calculate the sensible (H) and latent heat ($L_v E$) fluxes using the (a) optical microwave scintillation method and (b) eddy covariance method. The large arrows depict how the turbulent eddies are advected from their source area (footprint) to the scintillometer and EC sensor paths. Roman numerals I, II, and III represent the OMS calculations steps described in section 2b. A picture of every instrument is depicted next to the schemes.

$$C_{n,\text{opt}}^2 = C_{\text{opt}} D_{\text{opt}}^{7/3} L^{-3} \sigma_{\ln(I)}^2, \quad \text{and} \quad (1)$$

$$C_{n,\text{mw}}^2 = C_{\text{mw}} F_{\text{mw}}^{7/3} L^{-3} \sigma_{\ln(I)}^2, \quad (2)$$

where F_{mw} corresponds to the Fresnel length scale ($F = \sqrt{\lambda L}$), D_{opt} is the optical scintillometer aperture diameter (0.15 m), and C_{opt} (0.907) and C_{mw} (3.425) are coefficients determined for each experimental setup and rely on the ratio between F and D (e.g., Ward et al. 2015).

The second processing step determines the structure parameters of temperature, C_T^2 ($\text{K}^2 \text{m}^{-2/3}$), and water vapor, C_q^2 [$(\text{kg kg}^{-1})^2 \text{m}^{-2/3}$] (step II in Fig. 1a), where the wavelength-dependent structure parameter of the refractive index ($C_{n,\lambda}^2$), can be expressed as follows (Hill 1997):

$$C_{n,\lambda}^2 = A_{T,\lambda}^2 \frac{C_T^2}{T^2} + A_{q,\lambda}^2 \frac{C_q^2}{q^2} + 2A_{T,\lambda} A_{q,\lambda} \frac{C_T q}{T q}, \quad (3)$$

where $A_{T,\lambda}$ and $A_{q,\lambda}$ are dimensionless coefficients that depend on wavelength, pressure, temperature, and specific humidity (Ward et al. 2013). Two versions of Eq. (3) can be defined, i.e., one for the LAS ($\lambda = 880 \text{ nm}$) and one for the MWS ($\lambda = 1.8 \text{ mm}$). Equation (3), however, contains three unknown variables (C_T^2 , C_q^2 , and C_{Tq}), so a third expression is needed to solve the equations. Here, two approaches can be

followed. The first one is a method introduced by Lüdi et al. (2005), which uses the covariance between the LAS and MWS intensity fluctuations. This defines a cross structure parameter of the refractive index between the two wavelengths used, $C_{n,\text{opt,mw}}$. Thus, a third expression of Eq. (3) is provided, which allows us to solve the three unknowns. The method provided by Lüdi et al. (2005) is quite sensitive to errors in the correlation measurement. Therefore, we used the second method, elaborated by Hill (1997). This method prescribes a value for r_{Tq} , the correlation coefficient between temperature and humidity, which is related to C_T^2 and C_q^2 . The advantage of the Hill method is that the calculations are more robust, i.e., less sensitive to measurement errors, but good representative values for r_{Tq} must be known a priori (Stoffer 2018). Following the Hill method, the solution for C_T^2 and C_q^2 from Eq. (3) is given by

$$C_T^2 = \left(A_{q,\text{mw}}^2 C_{n,\text{opt}}^2 + A_{q,\text{opt}}^2 C_{n,\text{mw}}^2 + 2A_{q,\text{opt}} A_{T,\text{mw}} r_{Tq} \sqrt{C_{n,\text{opt}}^2 C_{n,\text{mw}}^2} \right) \frac{T^2}{\gamma^2}, \quad (4)$$

$$C_q^2 = \left(A_{T,\text{mw}}^2 C_{n,\text{opt}}^2 + A_{T,\text{opt}}^2 C_{n,\text{mw}}^2 + 2A_{T,\text{opt}} A_{T,\text{mw}} r_{Tq} \sqrt{C_{n,\text{opt}}^2 C_{n,\text{mw}}^2} \right) \frac{q^2}{\gamma^2}, \quad (5)$$

where $\gamma = A_{T,\text{mw}}^2 A_{q,\text{opt}}^2 - A_{T,\text{opt}}^2 A_{q,\text{mw}}^2$.

The third and last processing step is to connect C_T^2 and C_q^2 to the surface fluxes in the framework of MOST (step III in Fig. 1a), which states that turbulence variables can be made dimensionless using MOST scaling variables as a function of the stability parameter z/L_{ob} :

$$f_{C_T^2}(z/L_{ob}) = \frac{z^{2/3} C_T^2}{\theta_*^2}, \quad (6)$$

$$f_{C_q^2}(z/L_{ob}) = \frac{z^{2/3} C_q^2}{q_*^2}, \quad (7)$$

where θ_* and q_* are turbulent scaling variables for temperature and specific humidity and z/L_{ob} is a dimensionless stability parameter where z is the measurement height and L_{ob} the Obukhov length. $f_{C_T^2}$ and $f_{C_q^2}$ are empirical functions that have the following base shape for unstable conditions (Wyngaard et al. 1971):

$$f_{C_X^2} = c_1 \left(1 - c_2 \frac{z}{L_{ob}} \right)^{-2/3}, \quad (8)$$

where X stands for T or q . Parameters c_1 and c_2 are coefficients that depend on stability and are considered universal when the standard assumptions for MOST of homogeneous and isotropic turbulence are met. However, no unanimity exists on the universality of $f_{C_T^2}$ and $f_{C_q^2}$ coefficients (Beyrich et al. 2012), which indicates that MOST assumptions are often violated. Kooijmans and Hartogensis (2016) provided an overview of the coefficients and reported in the literature and they proposed their own values based on eleven data field experiments performed with the same instrumentation and with uniform data processing (see Table 2).

Sensible heat flux is determined as defined by the MOST framework as $H = -\rho c_p u_* \theta_*$, where ρ is the air density, c_p the specific heat capacity at constant pressure, u_* the friction velocity. Here, θ_* is solved iteratively from Eq. (7) in conjunction with expressions for the friction velocity u_* taken from standard flux profile relationships and the definition of the Obukhov length L_{ob} , given by

$$u_* = \frac{kU}{\ln\left(\frac{zU}{z_0}\right) - \Psi_m\left(\frac{z}{L_{ob}}\right) + \Psi_m\left(\frac{z_0}{L_{ob}}\right)}, \quad \text{and} \quad (9)$$

$$L_{ob} = \frac{Tu_*^2}{kg\theta_*}, \quad (10)$$

respectively, where k is the von Kármán constant (taken as 0.4), U is the wind speed measured at z , z_0 is the surface roughness length, Ψ_m are stability correction functions (Businger et al. 1971; Dyer 1967), T is the air temperature, and g is the gravity acceleration. Once u_* and L_{ob} are solved as part of the sensible heat flux calculation, we can solve q_* directly from Eq. (7) and from there on, the latent heat flux follows from its definition in the MOST framework ($L_v E = \rho L_v u_* q_*$).

The OMS data were processed from raw data to fluxes, according to the steps outlined in Fig. 1a. The raw 1-kHz intensity signals were filtered using a high-pass filter (31 s for the

LAS and 71 s for the MWS for low crosswind conditions and 10 and 20 s for high crosswind conditions, respectively) to avoid the contribution of absorption fluctuations to the scintillation statistic, $\sigma_{\ln(I)}^2$. Structure parameters of T and q were calculated according to the methodology proposed by Hill (1997) where we assumed, based on the EC measurements, the values of r_{Tq} were +0.7 for the day and +0.3 for the night. The $r_{Tq} = +0.7$ is a typical daytime value reflecting the strong correlation between T and q fluctuations as they are mostly being transported by the same turbulent eddies. The positive r_{Tq} values for the nighttime are atypical, which is caused by small, but positive H and $L_v E$ during the nighttime. Additionally, we used A_T and A_q coefficients (Ward et al. 2015) evaluated with data from a Vaisala WXT520 all-weather sensor which was supplied with the Radiometer Physics GmbH (RPG) MWS. We used the internal data acquisition system of the RPG-MWS receiver to record the raw OMS (LAS and MWS) data (see also section 3a). The data processing was made using our own code in MATLAB and Python scripts, following the steps depicted in this section. Fluxes were computed using the MOST functions for unstable conditions defined by Kooijmans and Hartogensis (2016), but also using site-fitted MOST functions presented in the results section. Parameter z_0 was solved from the wind flux profile relations [Eq. (9)] with prescribed u_* from the EC systems [see section 3b(4)]. The OMS fluxes were calculated at a temporal resolution of 10 min.

c. EC fluxes

EC data were processed using the flux software package EddyPro v6.2.2 (Fratini and Mauder 2014) from LI-COR Biosciences Inc. (Lincoln, Nebraska, United States) to obtain the turbulent fluxes of latent and sensible heat, and the momentum at a temporal resolution of 10 min. All necessary standard data treatment and flux correction procedures were included, such as axis rotation with the planar-fit procedure (Wilczack et al. 2001), raw data screening including spike removal (Vickers and Mahrt 1997), interval linear detrending, and low-pass filtering correction (Massman 2000). Structure parameters from EC data were estimated using the structure-function equation (Hartogensis 2006): $C_X^2 = [x(r_1) - x(r_2)]^2 / r_{1,2}^{2/3}$ with $x = q$ or T . The spatial separation $r_{1,2}$ was approximated through the wind speed and time step ($U\Delta t$) using nominal values of 0.5 and 1 m. An average C_X^2 for the two separation distances was used in this analysis. For a more detailed explanation of the eddy covariance instrumentation and data processing, see Suarez et al. (2020) and Lobos-Roco et al. (2021).

d. OMS and EC footprints

To quantify the source area that determines the measurements over heterogeneous surfaces, a footprint model is a useful tool (Meijninger et al. 2002). In simple words, it represents the “field view” of an instrument defined by an upwind area as a function of measurement height (Schuepp et al. 1990), the current wind regime, surface fluxes and characteristics (Leclerc and Foken 2014). Footprints are especially relevant when measurements are performed below the so-called blending height (Wieringa 1976). The footprints are calculated using the advection-diffusion model proposed by Horst and Weil (1992), which was derived

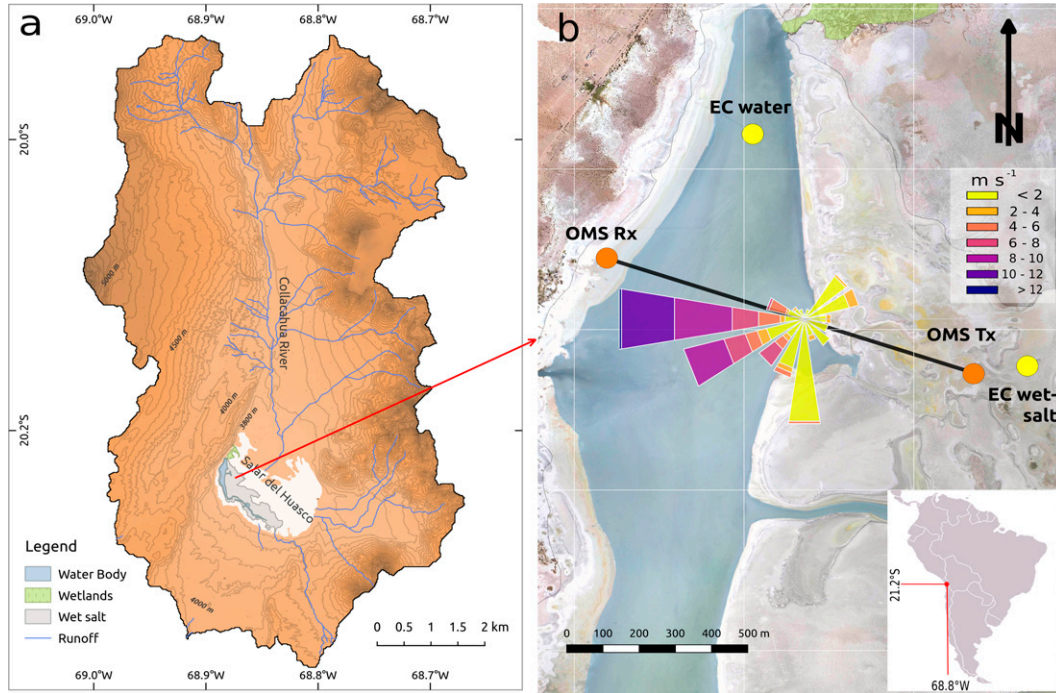


FIG. 2. Study area. (a) Salar del Huasco basin and saline lake. (b) Installation of the OMS and EC systems. Orange circles represent the OMS receiver (R_X) and transmitter (T_X), solid black line the OMS path and yellow circles the EC systems. Windrose indicates wind speed and direction of 15 Nov 2018.

for a point measurement such as the EC method. To extend this to a scintillometer path footprint, the path between transmitter and receiver is discretized in N steps, where the point footprint at each location x_i is convoluted with the path weighting function (Hartogensis et al. 2003) of the LAS and MWS (Meijninger et al. 2002) resulting in a representative source or footprint area (S_{path}):

$$S_{\text{path}} = \sum_{i=1}^N W_{\text{path}}(x_i) S_{\text{point}}\left(x_i, y, z, \frac{z}{L_{\text{ob}}}, U, \sigma_v\right), \quad (11)$$

where S_{point} represents the point-source function (Neftel et al. 2008) as a function of the horizontal positions x_i and y , the measurement height z , the Monin–Obukhov dimensionless stability parameter z/L_{ob} , the wind speed U , and σ_v as the standard deviation of the lateral wind speed component that is used to model the Gaussian lateral spread. Finally, the footprints have been truncated to a 95% cumulative contribution.

3. Site and data description

This section describes the E-DATA experiment where our OMS and EC data were gathered. Moreover, we provide a detailed description of the atmospheric and surface conditions observed during the E-DATA experiment expressed by the boundary layer development, wind regime, surface heterogeneity, footprints, and roughness length.

a. E-DATA experiment

The data used in this study were gathered during the E-DATA experiment (Suarez et al. 2020; Lobos-Roco et al.

2021) performed at the saline lake of the Salar del Huasco (20.2°S, 68.8°W, 3790 m MSL) in the Altiplano of the Atacama Desert from 13 to 24 November 2018. The Salar del Huasco is representative of a typical natural hydrological system of the Altiplano region of Chile, characterized by a closed basin surrounded by complex topography of volcanic origin (Fig. 2a). Its hydrological functioning is given by the balance between occasional convective showers in the summer and a long dry season during the rest of the year (de la Fuente et al. 2021). Even so, these basins sustain permanent wetlands and feed the saline lake continuously with water through seepage from a complex hydrogeological system, making Salar del Huasco one of the few pathways of evaporation in the region (Blin et al. 2021).

E-DATA was designed to study the evaporation in arid environments at local and regional scales over heterogeneous surfaces (Suarez et al. 2020). Part of the experiment was to collect data with an OMS installed over a ~15-cm-deep saline lake in the middle of the salt flat (see Fig. 2b). The OMS was in operation from 13 to 24 November 2018. We experienced problems with the data collection for two reasons. First, there were technical problems with the storage of the raw data. The internal computer of the RPG-MWS receiver was not powerful enough to store the raw data at 1 kHz, which resulted in only 20%–35% of the samples being stored with no information on the nature of the gaps. The consequence of this is that we were not able to analyze the spectra of the raw scintillation signal to exclude potential influence of absorption fluctuations that are supposedly filtered out by the aforementioned high-pass filter and the potential influence tripod vibrations in high-wind conditions (Aguirre et al. 2022). If not filtered out adequately both

TABLE 1. Sensors and variables measured by the OMS and EC in the E-DATA experiment: large aperture scintillometer (LAS), microwave scintillometer (MWS), structure parameter of temperature (C_T^2) and humidity (C_q^2), sensible heat flux (H), latent heat flux (L_vE), friction velocity (u_*), air temperature (T), ~5-cm temperature (T_S), relative humidity (RH), air pressure (p), parallel wind component (u), lateral wind component (v), vertical wind component (w), specific humidity (q), potential temperature (θ), incoming shortwave ($S_w\downarrow$), outgoing shortwave ($S_w\uparrow$), incoming longwave ($L_w\downarrow$), outgoing longwave ($L_w\uparrow$) radiation, and net radiation (R_n).

Instrument	Sensor	Variable measured	Variable estimated	Height (m)	Measurement frequency	Manufacturer
OMS	LAS	C_T^2	H	2.1	1 min	Kipp and Zonen
	MWS	C_q^2	L_vE	2.1		RPG
	WXT520	T , RH, p , u , v	u_*	2.7		Vaisala
EC _{water}	IRGASON	u , v , w , T , T_S , q	H , L_vE	1	10 min	Campbell Scientific
	CNR4	$S_w\downarrow$, $S_w\uparrow$, $L_w\downarrow$, $L_w\uparrow$	R_n	1	10 min	Kipp and Zonen
EC _{wet-salt}	IRGASON	u , v , w , T , T_S , q	H , L_vE	1.5	10 min	Campbell Scientific
	NR-Lite2	R_n	—	1.5	10 min	Kipp and Zonen
Radiosonde	iMet-4	T , RH, p , u , v	θ , q	0–2000	3 h	InterMet System Inc.

these effects lead to an increase in $\sigma_{\ln(I)}^2$ when the atmospheric conditions are favorable for these effects, i.e., a slow fluctuating humidity field and strong winds. As a result, the fluxes will be overestimated. Second, after 2.5 days into the experiment, the level of $\sigma_{\ln(I)}^2$ increased by a factor of 4 and stayed at that level for the rest of the experiment. We hypothesize that misalignment of the beam caused ground reflections and subsequently double the amount of scintillations observed, which would increase the scintillation statistic by a factor of 4. We attribute the slight misalignment to the soft, unstable wet-salt and mud surface. The result was that we had one day with acceptable data left (15 November 2018) with overlapping OMS and EC data. This is a restriction but, as reported by [Suarez et al. \(2020\)](#) and [Lobos-Roco et al. \(2021\)](#), all days in the campaign showed very similar behavior in surface fluxes (see [Fig. 5](#)). Therefore, we are confident that what we learned from our one golden day is representative of a typical day in late spring in our study area.

[Table 1](#) and [Fig. 2b](#) show the specific details of the OMS and EC systems installed. The OMS pathlength between the transmitter (T_x : 20.283°S, 68.870°W) and receiver (R_x : 20.280°S, 68.880°W) was 1070 m. We intended to place the OMS transmitter and receiver close to the shoreline ensuring an all-water footprint. In the end, we chose to install the OMS some distance from the shorelines where there was a somewhat higher (1 m) and firmer waterlogged wet salt. In all, the OMS path covered 300 m of wet salt and 770 m of water. The path crossed the saline lake from the northwest to southeast, offset northward by 45° with respect to the main wind speed ([Fig. 2b](#)). The transmitter and receiver were placed at 1.8 m above the wet salt, which was 0.5 m higher than the water surface, resulting in an OMS beam height of 2.3 m above the water. It is noteworthy to mention that the MWS beam size in the middle of the path, marked by the Fresnel length, reached 1.4 m, indicating that a minor misalignment could already give rise to ground reflections of the MWS beam. In addition, EC systems were installed over the lake (20.277°S, 68.882°W) and over a wet-salt surface (20.283°S, 68.875°W). Finally, to connect the analysis of the surface fluxes with the ABL dynamics, radiosondes were launched on 19 November 2018 at 0900, 1200, 1500, and 1800 LT from the lake surroundings (20.35°S–68.90°W; 3953 m MSL). The radiosondes were launched for measuring

vertical profiles of potential temperature (θ) and specific humidity (q) within the first 2 km from the surface.

b. E-DATA atmospheric and surface conditions

This subsection describes the atmospheric and surface conditions observed during the E-DATA experiment to provide a context for interpreting the scintillometer flux measurements. We will focus on two aspects. First, we will focus on the nonlocal processes associated with the regional atmospheric circulation that affect the atmospheric boundary layer development through advection and entrainment. Second, we will focus on the surface heterogeneity between water and wet salt in terms of near-surface temperature, net radiation, surface fluxes, roughness length, and how these areas are represented in the OMS footprint.

1) ATMOSPHERIC BOUNDARY LAYER

The nonlocal processes that define the land–atmosphere exchange in the Salar del Huasco are governed by a regional circulation pattern between the wet, cool, and low-elevation Pacific Ocean and the dry, hot, and high elevation of the Atacama Altiplano where the Salar del Huasco is located. This circulation is responsible for the two well-marked wind regimes observed over the entire Salar basin during the experiment ([Fig. 3](#)). The first wind regime corresponds to the relatively calm conditions that occur in the morning (0600–1200 LT) and is characterized by low wind speeds ($<2 \text{ m s}^{-1}$). During this regime, there is not a prevalent wind direction. The second wind regime corresponds to strong turbulent conditions that occur from noon onward (1200–2100 LT), which are characterized by high wind speeds ($>10 \text{ m s}^{-1}$). During this regime, there is a predominant westerly wind direction (250°–290°). The nature of this well-defined circulation has been analyzed in detail using observations and regional-scale modeling studies ([Lobos-Roco et al. 2021](#); [Suarez et al. 2020](#); [Munoz et al. 2018](#); [Rutllant et al. 2003](#)).

[Figure 4](#) shows the diurnal evolution of the potential temperature θ (top panels) and the specific humidity q (bottom panels) vertical profiles within the ABL. These profiles show a thermally stable ABL at 0900 LT, which rapidly develops to 1800 m at 1200 LT, becoming ~15 K warmer with respect to the morning. The morning boundary layer development is

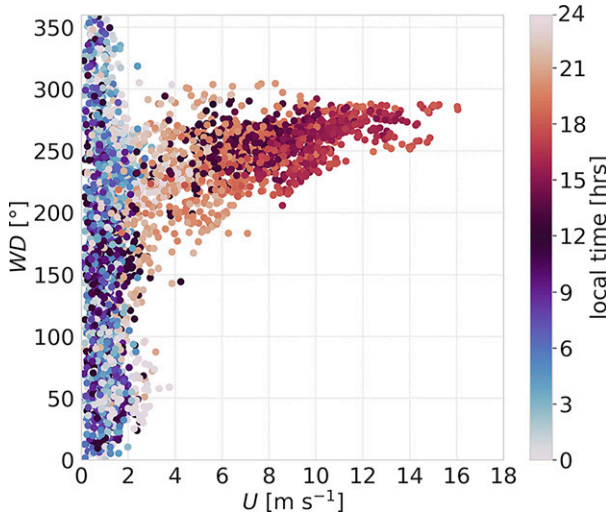


FIG. 3. Diurnal relationship between wind speed (U) and wind direction (WD) obtained by EC over water and wet-salt surfaces.

dominated by the surface and entrainment fluxes leading to a reduction of the inversion layer jump to ~ 1 K. The rapid boundary layer growth is interrupted after midday, where the ABL decays abruptly to 500 m. The decrease in the ABL height is associated with the advection of relatively cold air from the Pacific Ocean to the study area by a regionally driven wind regime introduced in Fig. 3 (see also Lobos-Roco et al. 2021; Suarez et al. 2020).

A similar pattern is observed for moisture in the bottom panels of Fig. 4. Here, a layer with a negative humidity gradient grows fast in the morning until it is interrupted in the early afternoon by the regional flow. The moisture profile shows that the air in the shallow boundary layer caused by the regional flow is relatively moister, i.e., we observe an increase of the specific humidity from <1 to 3.5 g kg^{-1} .

2) SURFACE HETEROGENEITY

To demonstrate the level of surface heterogeneity of the area covered by the OMS and EC measurements, we show time series of near-surface temperature, net radiation (R_n), and turbulent surface fluxes measured at the EC stations over the water and wet-salt surfaces (Fig. 5). In general terms, during the day, the near-surface (~ 5 -cm height) temperature is lower for the water surface (see Fig. 5b), so less longwave outgoing radiation will be lost to the atmosphere. In addition, a considerably higher albedo is observed over the wet salt (0.58) compared to the water surface (0.12) (Lobos-Roco et al. 2021). As a result of the differences in surface temperature and albedo during the afternoon, much more radiation energy is available at the water's surface, which shows maximum values of $\sim 900 \text{ W m}^{-2}$ compared to the maximum values of $\sim 500 \text{ W m}^{-2}$ over the wet-salt surface. These remarkable differences in R_n have repercussions in the partitioning of the sensible and latent heat fluxes. Figures 5a and 5b also show the surface fluxes of latent heat ($L_v E$) and sensible heat (H) over wet salt and water averaged along the E-DATA period. The first characteristic observed is the day-to-day low variability (shades) in the surface fluxes, evidence that the same diurnal cycle occurs every day. Even though both surfaces are water saturated, their flux characteristics are completely different. To begin with, the fluxes over the wet salt are smaller by a factor of ~ 3 compared to the water surface given the much-reduced amount of net radiation available. In addition, $H > L_v E$ for the wet salt, whereas $L_v E > H$ for the water surface. This is remarkable since the wet salt crust is waterlogged. The hypersalt concentrations, however, impede the water escaping from the surface (e.g., Salhotra et al. 1985; Oroud 1999). As a result, most of the energy is dedicated to heating the air. Two aspects are equal for both surfaces. First is the sudden increase of fluxes at 1200 LT aligned with the arrival of the strong winds that break the virtually absent turbulent mixing seen in the morning (Lobos-Roco et al. 2021). Second is

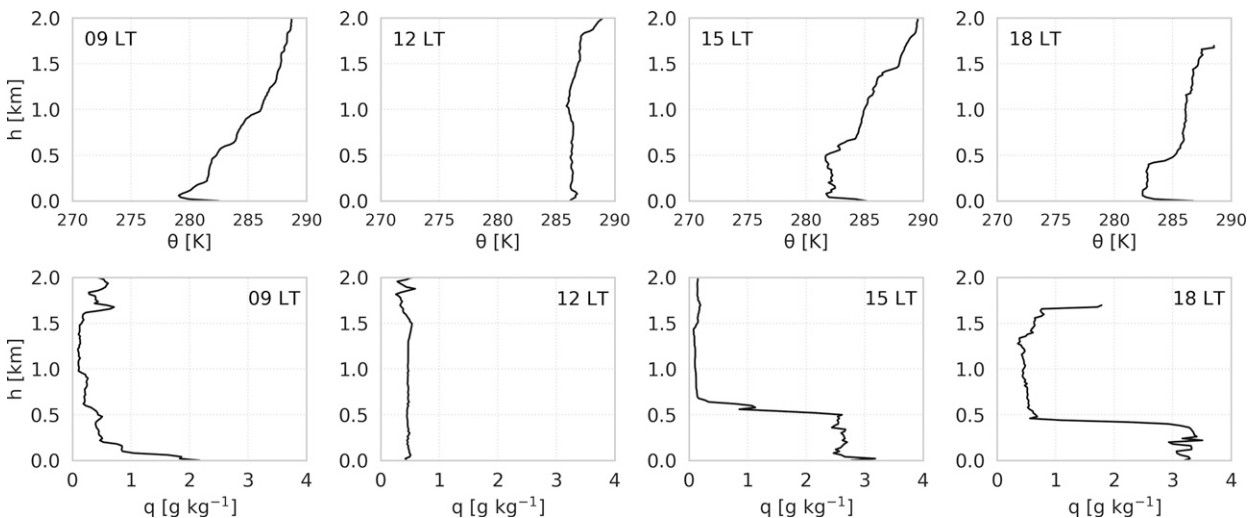


FIG. 4. Atmospheric boundary layer conditions measured during E-DATA on 19 Nov 2018. (top) Diurnal cycle of the potential temperature radiosounding profiles. (bottom) Diurnal cycle of specific humidity radiosounding profiles.

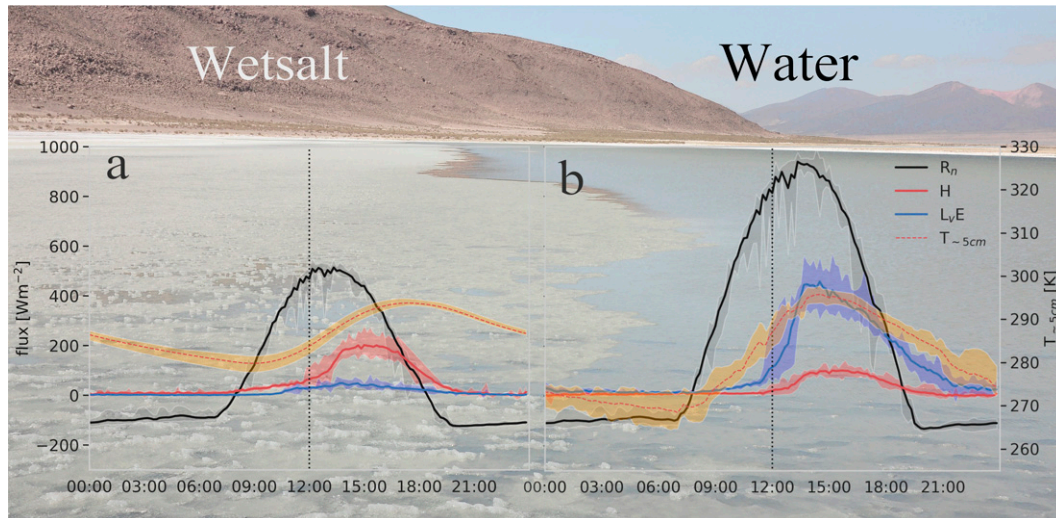


FIG. 5. Diurnal-averaged time series of near-surface (~ 5 cm) temperature, net radiation, and turbulent fluxes over the (a) wet-salt and (b) water surfaces during the E-DATA period. The picture behind exemplifies the wet-salt and water surface during the experiment. Shades indicate the minimum and maximum values across the E-DATA period.

the positive sensible heat flux during both the day and night, meaning that the atmosphere is unstable even during nighttime conditions. Lobos-Roco et al. (2021) argue that the unstable nighttime condition is related to a katabatic flow that drains cold air from the surrounding mounting ridges into the Salar. However, it also might be related to the high heat capacity of the surface, causing heating of near-surface air further into the night.

3) FOOTPRINT ANALYSIS

The source area or footprint is highly dependent on the wind regime (Fig. 3). Figures 6a–d shows the footprints for both scintillimeters (LAS and MWS) and the EC systems (water and wet salt) at two representative times of each wind regime (0900 and 1600 LT, respectively). The footprints have been truncated to a 95% cumulative contribution. Both scintillometer and EC footprints are considerably smaller in the morning compared to the afternoon due to the different wind and related flux regimes. Their orientation changes according to the wind direction. Under all conditions, the EC footprints cover only a small portion of the surface above which they are installed (Table 1). The scintillometer footprints, on the other hand, always cover a mix of both water and wet salt. On average, about 2/3 of the LAS and MWS footprints are covered by water and 1/3 wet salt. The difference in the path weighting function means that the LAS footprints are more weighted toward the center of the path (Evans and De Bruin 2011) and therefore cover a slightly larger area of water compared to the MWS footprints.

This systematic difference can also be seen in Fig. 6e, which expresses the time-dependent footprint proportions covering water and wet salt for the two scintillimeters on 15 November 2018. Driven by the wind regimes, we observe two distributions of footprints. During daytime when the winds are generally from the west and they

become strong during the afternoon, the distribution is roughly 80% water and 20% wet salt. In the evening and night, the contributions of both surfaces to the scintillometer footprints are much more variable depending on the wind direction with contributions from water varying between 50% and 80% and wet salt between 20% and 50%. The diurnal cycle of the OMS water/wet-salt footprint proportion is only relevant when surface fluxes observed over both water and wet-salt surfaces are significantly different (Fig. 6e). The strong difference in flux regimes between the two surfaces demonstrates the importance of constructing a footprint-weighted composite of the EC fluxes when comparing them with those of the scintillimeters.

4) ROUGHNESS LENGTH

For the OMS flux calculations, an accurate estimate of z_0 , is crucial given the fact the measurements were conducted close to the surface (~ 2 -m height) and the afternoon winds were strong. Under these conditions, mechanically generated turbulence is a key process in determining the fluxes [see Eqs. (7)–(10)]. The wet-salt and water surfaces are very smooth, and an appropriate z_0 estimate is, therefore, not trivial. We solved z_0 from the wind flux profile relation [Eq. (9)] using the estimates of U , u^* , and from the EC stations of water and wet salt. The results, presented in Fig. 7, show that for low wind speeds, z_0 is ill defined and for high wind speeds, its value converges to a value indicated by the solid lines (Mahrt et al. 2001). On average, the water surface is smoother with $z_0 = 4 \times 10^{-5}$ m against $z_0 = 2 \times 10^{-4}$ m for the wet-salt surface. The shallow water becomes choppy in the afternoon, but this is not intense enough to cause z_0 to be a function of wind speed (Charnock 1955). A weighted value considering the typical afternoon footprints over these two surfaces yields a value of $z_0 = 1.5 \times 10^{-4}$ m that we used in the flux calculations.

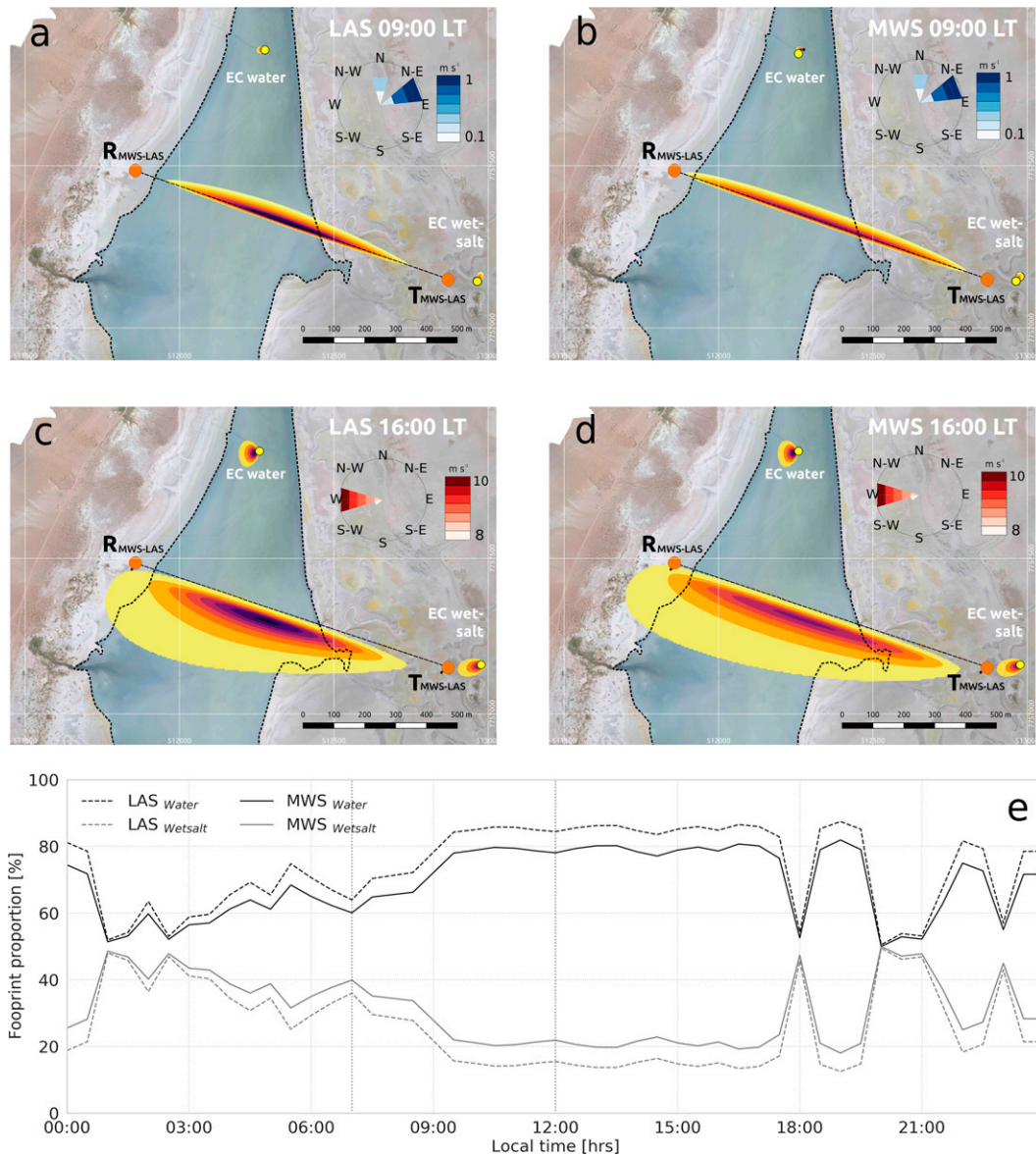


FIG. 6. Footprints of the (a),(c) LAS and EC and (b),(d) MWS and EC over the water and wet-salt surfaces for representative hours of wind regimes on 15 Nov 2018. Colors (given without scale) represent the percentage contribution of that area to the total footprint. The wind roses characterize the wind regimes for the same day (top) between 0700 and 1200 LT and (middle) between 1200 and 2000 LT. The background image is a georeferenced mosaic based on a drone flight on 18 Nov 2018. (e) Diurnal cycle of LAS and MWS percentage footprint contributions from the water (solid lines) and wet-salt surface (dotted lines).

4. Results and discussion

a. MOST functions

To assess the representativity of MOST for the special conditions in the Salar del Huasco, Fig. 8 shows the C_T^2 and C_q^2 dimensionless groups [Eqs. (6) and (7)] as a function of z/L_{ob} for EC-based structure parameters (Figs. 8a,b) and OMS structure parameters (Figs. 8c,d). The EC-based structure parameters are composed values from the wet-salt and water EC systems and reflect data from the entire 10-day

E-DATA experiment, whereas the OMS structure parameters only include data from 15 November 2018. The data points in Fig. 8 were filtered by excluding values for which $|H| < 5 \text{ W m}^{-2}$. In addition, in Figs. 8a and 8b the C_T^2 and C_q^2 dimensionless groups were filtered to the 25%–75% inter-quartile range. The structure parameters from the EC systems along with the EC-flux-derived variables θ_* , q_* , and L_{ob} are weighted by the OMS water/wet-salt footprint proportions (wfp subscript). The data points are marked by the wind regime where, not surprisingly, the points associated

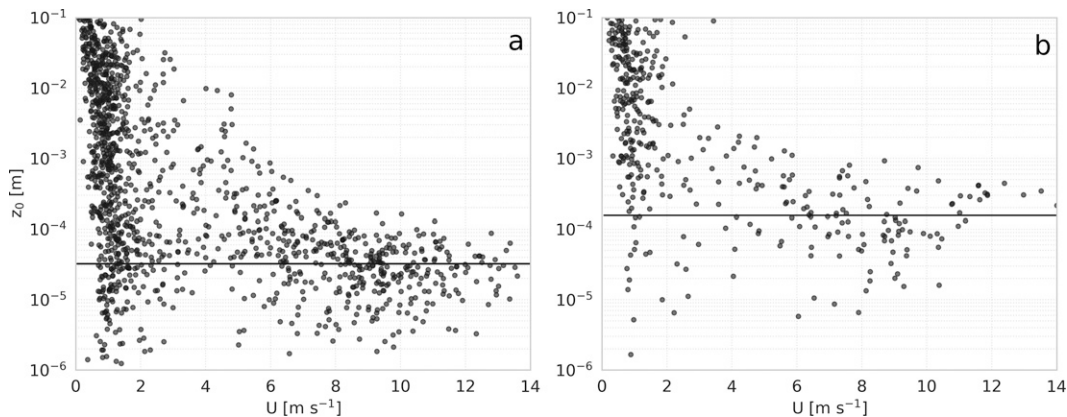


FIG. 7. Relationship between roughness length (z_0) and wind speed over (a) water surface and (b) wet-salt surface. Wind speed data are taken from the EC systems. The solid lines express the values to which z_0 converges for high wind speeds.

with the strong wind conditions are on the neutral side of the $-z/L_{\text{ob}}$ range.

Figure 8a shows that standard MOST functions slightly overestimate the C_7^2 data points during the windy regime, but data are well represented during the calm wind conditions. Likewise, Figure 8b shows that standard MOST functions represent both windy and calm regimes well for the C_q^2 dimensionless group data points. Figure 8c shows that for C_7^2 , the standard MOST functions of Kooijmans and Hartogensis (2016) cover the data points reasonably well under both wind regimes. However, for C_q^2 (Fig. 8d), the data points follow the standard MOST functions during the calm regime, whereas for the windy regime, the data points are far above both the Kooijmans and Hartogensis (2016) function and the EC data points (shown in Fig. 8b). As our dataset did not allow us to discard the influence of instrumental issues that might explain the elevated OMS C_q^2 we will, for the sake of the argument, assume that they do not play a role and discuss a physical process that plays a role here. The OMS and EC measure below the blending height. As the EC footprints are entirely above water and wet-salt surfaces (Fig. 6), no interaction between their respective internal boundary layers affects the measurements. However, in the case of OMS, 2/3 of the footprint is covered by water and 1/3 by wet salt, with an order of magnitude difference of $L_v E$ flux regime (Fig. 5). This high contrast contributes to having strong humidity fluctuations within the internal boundary layers at the transition between the two surfaces, elevating the measured C_q^2 by the OMS. For C_7^2 (Fig. 8c), higher values are observed for the OMS as compared to the EC. However, the difference is less pronounced since the contrast between H flux surfaces is less as well. Note that both EC and OMS are under a setting governed by a regional advection and entrainment of air not originating from the Salar (Lobos-Roco et al. 2021). Such regional circulation contributes to 40% of the total diurnal moisture budget above the water surface and this phenomenon might cause additional humidity fluctuations. However, our data do not show evidence of this since we observe high differences between the C_q^2 of EC and OMS, where the same conditions are supposed to affect both instruments. It is also under these

conditions of no horizontal homogeneity and regional advection that MOST fails.

To mitigate these effects, we adopted a practical approach to eye-fit an alternative C_q^2 MOST relation that inherently considers the enhanced C_q^2 . Our motivation to use an eye-fit rather than a statistical approach, like the one performed by Kooijmans and Hartogensis (2016), is that we only have a single day of measurements available, whereas other methods require significant amounts of data. For C_7^2 , we use the coefficients determined by Kooijmans and Hartogensis (2016). The proposed line is depicted in Fig. 8d and the coefficients that define it are given in Table 2.

b. Impact of footprint and MOST on surface fluxes

In this section, we demonstrate that it is essential to consider the impacts of the footprint and MOST functions when comparing the performance of the OMS in a complex environment like the Salar del Huasco.

Figure 9 shows the diurnal cycle of surface fluxes measured by EC over water and wet-salt surfaces as well as the diurnal cycle combining both EC system fluxes, but weighting them using the OMS footprint (EC_{wfp}) presented in Fig. 6e. EC_{wfp} resembles most of the EC fluxes over water (80%) than wet salt (20% wet salt) during daytime. Given the high flux contrast between wet salt and water, the 20% wet salt seen in the OMS footprint significantly influences the composed fluxes. This is the case for $L_v E$, where during daytime, it is $\sim 75 \text{ W m}^{-2}$ over wet salt versus $\sim 550 \text{ W m}^{-2}$ over water, the EC_{wfp} $L_v E$ is $\sim 100 \text{ W m}^{-2}$ lower than that of the water surface. For the sensible heat flux (Fig. 9c), the absolute values of the fluxes are lower and the contrast between the two surfaces is less extreme resulting in an EC_{wfp} H that is only $\sim 10 \text{ W m}^{-2}$ higher than that of the water surface. The orthogonal regression (Figs. 9b,d) between EC water, wet salt, and wfp shows a quantification of the differences in $L_v E$ and H of water and wet salt with respect to EC_{wfp} .

When performing scintillometer measurements over heterogeneous terrain under the blending height (Wieringa 1976), the structure parameters of the individual surfaces within the

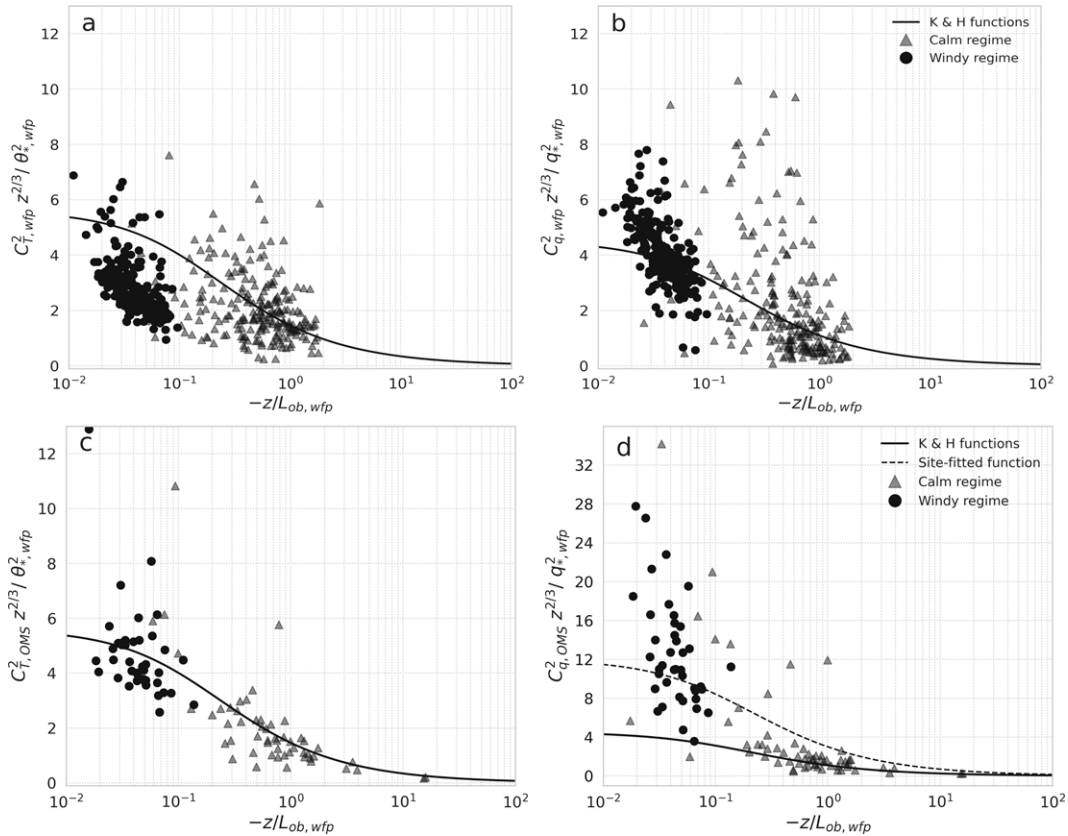


FIG. 8. Dimensionless C_T^2 and C_q^2 groups vs stability parameter (z/L_{ob}). (a),(b) C_T^2 and C_q^2 dimensionless group using parameters from EC water and wet salt weighted by the OMS footprint (wfp) during the E-DATA period. (c),(d) C_T^2 and C_q^2 dimensionless group using structure parameters measured by the OMS and the remaining parameters from EC water and wet salt weighted by the OMS footprint (wfp) during 15 Nov 2018. MOST functions proposed by Kooijmans and Hartogensis (2016) and the proposed ones in this study are shown in solid and dashed lines, respectively. The experimental data points are marked by their wind regime (windy $> 4 \text{ m s}^{-1}$ between 1300 and 2040 LT and calm $< 4 \text{ m s}^{-1}$ between 2340 and 1300 LT).

footprint will be sensed by the instrument (Meijninger et al. 2002). In our study, the OMS was installed close to the surface (2.3 m), and it is safe to assume we were below the blending height (Meijninger et al. 2002). Due to the nonlinear relationship between structure parameters and surface fluxes, there will be a difference between the EC flux weighted by the OMS footprint (EC_{wfp}), and the EC flux calculated using structure parameters weighted by the OMS footprint ($EC_{C_X, wfp}$) (Lagouarde et al. 2002; Meijninger et al. 2006). The latter more accurately simulates the way of measuring the OMS. To quantify the difference between the two approaches, we constructed the OMS footprint-weighted, indirect EC flux estimate through C_X^2 ($EC_{C_X, wfp}$).

TABLE 2. Kooijmans and Hartogensis (2016) MOST function coefficients for unstable conditions [base function in Eq. (8)]. Numbers in parentheses are the site-fitted coefficients for the Salar del Huasco study case, 15 Nov 2018 (Fig. 8d).

MOST functions	c_1	c_2
$f_{C_T^2}$	5.6	6.5
$f_{C_q^2}$	4.5 (12)	7.3 (7)

following these steps: 1) obtain C_T^2 and C_q^2 from the EC fluxes over water and wet salt applying an inverse MOST procedure using standard MOST function coefficients (Kooijmans and Hartogensis 2016); 2) construct simulated OMS-path-weighted structure parameters using the OMS-weighted footprint factors; and finally 3) calculate simulated OMS-path-weighted fluxes based from the path averaged structure parameters of step 2 using the same MOST functions of step 1.

Figure 10 shows the difference between the two approaches described above. The big contrast in C_q^2 between water and wet salt, connected to their contrast in $L_v E$ (see Figs. 5a,b) and the nonlinear relationship between C_q^2 and $L_v E$, causes a difference of $\sim 13\%$ between EC_{wfp} and $EC_{C_X, wfp}$. So, this is a significant factor to consider when validating OMS derived fluxes with a footprint composite of EC fluxes. For the sensible heat fluxes, the difference is negligible, which is related to the much smaller fluxes with less contrast between the two surfaces (see Fig. 5).

Next, we will look at the difference in OMS-derived fluxes with standard MOST functions [Eq. (8)] taken from Kooijmans and Hartogensis (2016) and site-fitted MOST functions as determined in Fig. 8 and Table 2. Figure 11

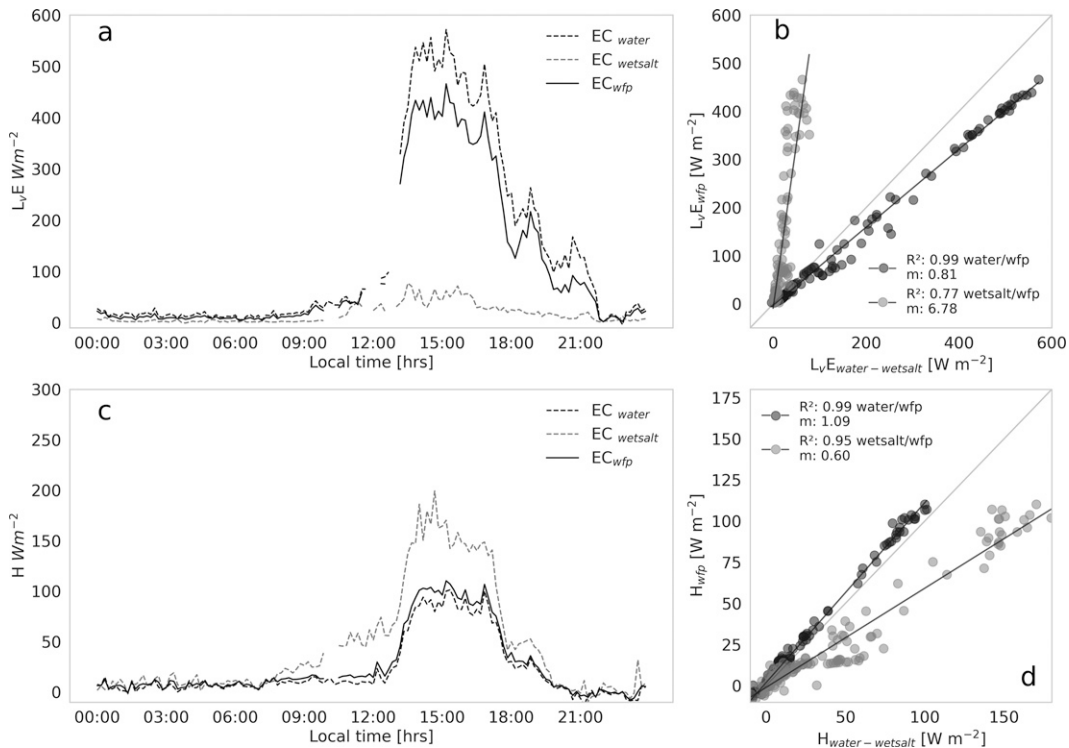


FIG. 9. Diurnal cycle of (a),(c) surface fluxes and (b),(d) orthogonal regression between EC over water and wet salt and an OMS footprint composed EC flux (EC_{wfp}) for 15 Nov 2018. The “m” indicates the regression slope; gray data points refer to wet salt and black ones to water.

shows an overestimation of L_vE (factor of 1.64) if standard MOST functions are used. This is a clear indication that MOST assumptions are violated in the Salar del Huasco basin. In part, this has to do with the surface heterogeneity, noting that we measured below the blending height and measurements were thus sensitive to the non-MOST turbulence behavior at the transition between the two contrasting surfaces in the OMS footprint. In addition, regional advection of dry air has a strong influence on the local humidity (Lobos-Roco et al. 2021). Consequently, the relationship between the measured humidity fluctuations and local fluxes do not follow the standard relationships.

Figure 12 brings together the results presented so far, i.e., OMS fluxes based on site-fitted MOST functions ($OMS_{site-fitted-MOST}$), and EC_{wfp} and $EC_{C_{x,wfp}}$ fluxes that serve as references. In general, we observe a reasonable agreement. The orthogonal regressions in Figs. 12b and 12d are based on $EC_{C_{x,wfp}}$ as this more closely resembles the OMS flux estimate given the fact that we measured below the blending height. After all the careful and guided treatment of the data, we arrive at zero-intercept linear regression with slope coefficients of 0.95 and 1.07 and correlation coefficients R^2 of 0.92 and 0.96 for L_vE and H , respectively.

5. Conclusions

This paper studies the performance of an optical microwave scintillometer (OMS) in measuring evaporation over a saline

lake in a heterogeneous setting in the Atacama Desert. Our research question, “How accurate can the measurements of an OMS over an open-water body be under arid conditions?”, was inspired by the possibility of the OMS to be installed at the borders of an open-water body. We conclude that the OMS is capable to measure open-water evaporation without the need to install instrumentation in the water. However, care must be taken to not include (unwillingly) surrounding areas with contrasting flux regimes in the OMS footprint. We argue that with measurements below the blending height an enhanced level of temperature and humidity fluctuations is observed. This is due to the passage of the scintillometer beam through the internal boundary layer that defines the transition between the different surfaces. As a result, Monin–Obukhov similarity theory (MOST) relations, needed to infer the sensible and latent heat fluxes from the measured structure parameters of temperature and humidity, can potentially fail. The OMS dependence on the MOST, which relies on the assumption of locally driven, undisturbed turbulence is a weakness that requires further study. We should also note that there also more trivial, instrumental issues that can cause MOST to fail, in the case of the OMS most notably are absorption fluctuations and tower or tripod vibrations.

For our study focusing on a saline lake in the Salar del Huasco, the OMS deployment proved to be challenging due to the unstable ground near the water edge. We therefore extended the path such that the instrument transmitter and

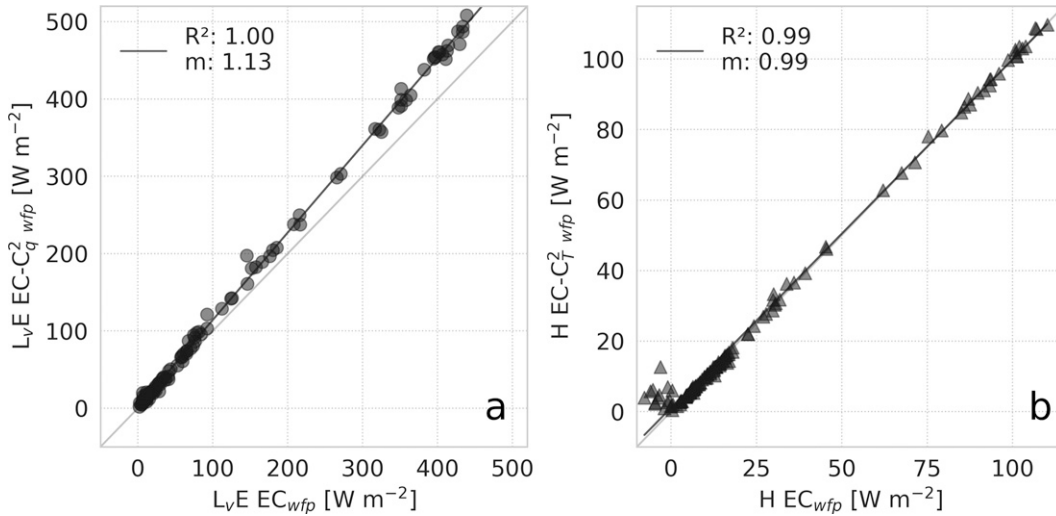


FIG. 10. Relationships of (a) latent and (b) sensible heat fluxes between OMS-footprint-weighted, direct EC flux estimates (EC_{wfp}) and indirect EC flux estimates through C_{χ}^2 ($EC_{C_{\chi}^2, wfp}$).

receiver were installed on stable ground with a waterlogged salt surface. The resulting scintillometer setup was defined by an installation height of 2.3 m, which can be considered below the blending height and a pathlength of 1070 m covering a mixed footprint of open water and a waterlogged salt surface with a daytime footprint coverage of $\sim 80\%$ and $\sim 20\%$, respectively. As a reference, we installed an EC system over the open water and one over the wet-salt surface. Even though both surfaces in the footprint were water saturated, they were strongly heterogeneous in their flux regimes due to their different evaporation properties. In short, the amount of available energy was much less over the wet-salt surface compared to the water surface (maximum R_n values of $900 W m^{-2}$ over water versus $500 W m^{-2}$ over the wet salt) due to the larger albedo and lower surface temperature. The salt also impeded evaporation leading to $H > L_v E$ in contrast to the water surface where $L_v E > H$. The large contrast in fluxes was especially visible in $L_v E$ values (maximum values of $75 W m^{-2}$ over wet salt versus $550 W m^{-2}$ over water). For H values, the contrast was also notable but much less pronounced (maximum values of $200 W m^{-2}$ over wet salt versus

$100 W m^{-2}$ over water). In addition to the local heterogeneity, the fluxes were governed by a regional wind-driven turbulence regime with a low-wind, low-flux regime during the night and morning and strong-wind, high-flux regime during the afternoon.

The mixed footprint setup including a transition between the heterogeneous surfaces marked by disturbed turbulence made that our evaluation of the OMS fluxes against those measured by EC focused on the following three points. In our evaluation of the OMS fluxes against those measured by EC we addressed the heterogeneous setting of the OMS measurements by critically evaluating the MOST functions, estimating an OMS footprint composing EC flux and discussing the regional-scale-driven turbulence regime. Concerning these three issues our main findings are as follows.

First, we evaluated the MOST functions used to infer the OMS measured structure parameters to fluxes. We did this for both the scintillometer as well as the EC data-derived structure parameters for temperature C_T^2 and humidity C_q^2 . Here, we found that for C_T^2 , our data correspond well to the standard MOST functions as determined by Kooijmans and

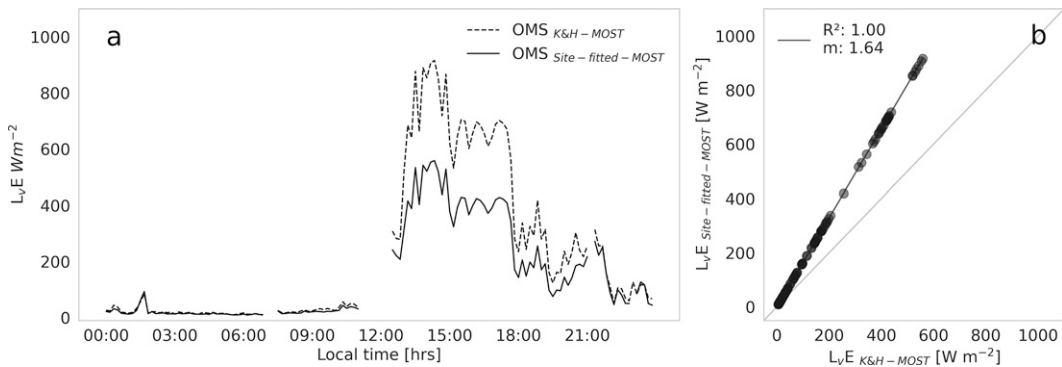


FIG. 11. (a) Diurnal cycle and (b) orthogonal regression of latent heat flux from OMS data calculated with standard and site-fitted MOST functions. m indicates the regression slope.

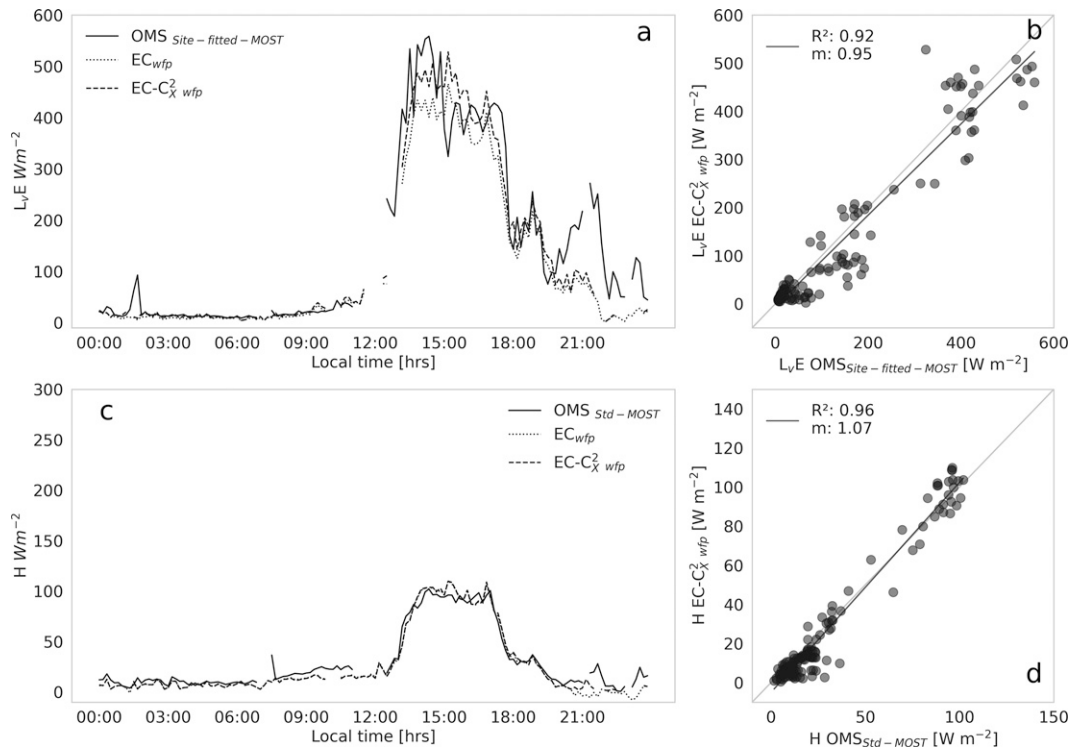


FIG. 12. Diurnal cycle of (a),(c) surface fluxes and (b),(d) orthogonal regression between the OMS with site-fitted MOST functions and OMS-footprint-weighted, direct EC flux estimates (EC_{wfp}) and indirect EC flux estimates through C_x^2 ($EC_{C_x^2, wfp}$). The “m” indicates the regression slope.

Hartogensis (2016), which was based on many experiments. For C_q^2 , however, we observe much higher OMS values than those based on the EC data. We attribute this to the aforementioned internal boundary layer disturbances at the transition between the surfaces. The OMS C_T^2 values are also somewhat higher than those from the EC data, but the difference is limited as the sensible heat flux contrast between the two surfaces is much less than that for C_q^2 . Again, instrument issues could be an explanation as well. We were, however, not able to fully discard this possibility as the recorded raw data stream missed 70% of the samples making a spectral analysis impracticable. To compensate for the elevated OMS C_q^2 values, we adopted a practical approach by using site-adapted MOST coefficients. We should note that our approach to adjust C_q^2 MOST functions to account for disturbances at the transition of the two heterogeneous surfaces assumes that the instrument was otherwise performing well. We applied a strict filtering of the available data. In the end, we only used one day of data as the other days showed unphysically high scintillation intensities, likely due to a minor misalignment that might have caused surface reflections of the beam. Also, we strictly high-pass filter the raw 1-kHz data to exclude potential absorption fluctuations. Here, we adopted filter constants depending on the wind regimes.

Second, following the approach by Meijninger et al. (2002) for scintillometer measurements performed below the blending height, we validated the OMS against a composed flux

consisting of OMS-footprint-weighted EC fluxes over the two surfaces. In addition, we considered the nonlinear relationship between structure parameters and surface fluxes in the footprint analysis that lead to an increase in EC composed L_vE of 15%. All things combined, we reach a zero-intercept linear regression with an R^2 of 0.92 and a slope of 0.95 when comparing the evaporation of the OMS against the OMS footprint composed EC estimates.

Third, we also discussed the influence of the regionally driven wind regime that controls the boundary layer development and turbulent mixing and is responsible for the advection and entrainment of dry air to the study area. These aspects influence both the EC and OMS measurements. Judging by the differences in structure parameters derived from the OMS and EC and how these influence the dimensionless MOST relations, it seems that the local MOST functions, in either the water or the wet salt, are not really affected by these nonlocal disturbances.

Finally, the weakness of the OMS method is its dependence on the Monin–Obukhov similarity theory, which relies on the assumption of locally driven fluxes. This assumption is often violated in (semi)arid regions where strong spatial contrasts in the temperature and humidity lead to temperature and humidity fluctuations that are driven by nonlocal processes such as regional circulations and internal boundary layers. Our approach was to introduce site-fitted MOST functions. We do not see this as a general solution but merely as a way to quantify the impact of the MOST violation. This is a

challenge that we must overcome for the OMS to be used as a standard method for evaporation over open-water bodies.

Acknowledgments. This research received financial support from the Chilean National Agency of Science and Development through the project ANID/FONDECYT/1210221. Support for Felipe Lobos-Roco was provided by the Wageningen University Ph.D. Sandwich Project 5160957644. F. Suárez acknowledges the support from the Centro de Desarrollo Urbano Sustentable (CEDEUS - ANID/FONDAP/15110020) and from the Centro de Excelencia en Geotermia de los Andes (CEGA - ANID/FONDAP/15200001).

Data availability statement. Data available at <http://dx.doi.org/10.17632/fkdzr7b5s6.1>.

REFERENCES

- Abtew, W., and A. Melesse, 2012: *Evaporation and Evapotranspiration: Measurements and Estimations*. Springer, 219 pp.
- Aguirre, F., O. Hartogensis, F. Meza, and F. Suárez, 2022: Refinements and analysis of the optical-microwave scintillometry method applied to measurements over a vineyard in Chile. *Water*, **14**, 474, <https://doi.org/10.3390/w14030474>.
- Beyrich, F., and Coauthors, 2012: Towards a validation of scintillometer measurements: The LITFASS-2009 experiment. *Bound.-Layer Meteor.*, **144**, 83–112, <https://doi.org/10.1007/s10546-012-9715-8>.
- Blin, N., M. Hausner, S. Leray, C. Lowry, and F. Suárez, 2021: Potential impacts of climate change on an aquifer in the arid Altiplano, northern Chile: The case of the protected wetlands of the Salar del Huasco basin. *J. Hydrol. Reg. Stud.*, **39**, 100996, <https://doi.org/10.1016/j.ejrh.2022.100996>.
- Businger, J. A., J. Wyngaard, Y. Izumi, and E. F. Bradley, 1971: Flux-profile relationships in the atmospheric surface layer. *J. Atmos. Sci.*, **28**, 181–189, [https://doi.org/10.1175/1520-0469\(1971\)028<0181:FPRITA>2.0.CO;2](https://doi.org/10.1175/1520-0469(1971)028<0181:FPRITA>2.0.CO;2).
- Charnock, H., 1955: Wind stress on a water surface. *Quart. J. Roy. Meteor. Soc.*, **81**, 639–640, <https://doi.org/10.1002/qj.49708135027>.
- de la Fuente, A., C. Meruane, and F. Suarez, 2021: Long-term spatiotemporal variability in high Andean wetlands in northern Chile. *Sci. Total Environ.*, **756**, 143830, <https://doi.org/10.1016/j.scitotenv.2020.143830>.
- Dyer, A., 1967: The turbulent transport of heat and water vapour in an unstable atmosphere. *Quart. J. Roy. Meteor. Soc.*, **93**, 501–508, <https://doi.org/10.1002/qj.49709339809>.
- Evans, J., and H. De Bruin, 2011: The effective height of a two-wavelength scintillometer system. *Bound.-Layer Meteor.*, **141**, 165–177, <https://doi.org/10.1007/s10546-011-9634-0>.
- , D. McNeil, J. Finch, T. Murray, R. Harding, H. Ward, and A. Verhoef, 2012: Determination of turbulent heat fluxes using a large aperture scintillometer over undulating mixed agricultural terrain. *Agric. For. Meteorol.*, **166**, 221–233, <https://doi.org/10.1016/j.agrformet.2012.07.010>.
- Frattini, G., and M. Mauder, 2014: Towards a consistent eddy-covariance processing: An intercomparison of EddyPro and TK3. *Atmos. Meas. Tech.*, **7**, 2273–2281, <https://doi.org/10.5194/amt-7-2273-2014>.
- Green, A., M. Astill, K. McAneney, and J. Nieveen, 2001: Path-averaged surface fluxes determined from infrared and microwave scintillometers. *Agric. For. Meteorol.*, **109**, 233–247, [https://doi.org/10.1016/S0168-1923\(01\)00262-3](https://doi.org/10.1016/S0168-1923(01)00262-3).
- Han, P.-F., X.-S. Wang, and J.-Z. Wang, 2019: Using large-aperture scintillometer to estimate lake-water evaporation and heat fluxes in the Badain Jaran Desert, China. *Water*, **11**, 2575, <https://doi.org/10.3390/w11122575>.
- Hartogensis, O. K., 2006: Exploring scintillometry in the stable atmospheric surface layer. Ph.D. thesis, Wageningen University, 240 pp.
- , C. Watts, J. Rodriguez, and H. De Bruin, 2003: Derivation of an effective height for scintillometers: La Poza experiment in Northwest Mexico. *J. Hydrometeorol.*, **4**, 915–928, [https://doi.org/10.1175/1525-7541\(2003\)004<0915:DOAEHF>2.0.CO;2](https://doi.org/10.1175/1525-7541(2003)004<0915:DOAEHF>2.0.CO;2).
- Hill, R., 1997: Algorithms for obtaining atmospheric surface-layer fluxes from scintillation measurements. *J. Atmos. Oceanic Technol.*, **14**, 456–467, [https://doi.org/10.1175/1520-0426\(1997\)014<0456:AFOASL>2.0.CO;2](https://doi.org/10.1175/1520-0426(1997)014<0456:AFOASL>2.0.CO;2).
- , S. Clifford, and R. S. Lawrence, 1980: Refractive-index and absorption fluctuations in the infrared caused by temperature, humidity, and pressure fluctuations. *J. Opt. Soc. Amer.*, **70**, 1192–1205, <https://doi.org/10.1364/JOSA.70.001192>.
- Horst, T., and J. Weil, 1992: Footprint estimation for scalar flux measurements in the atmospheric surface layer. *Bound.-Layer Meteorol.*, **59**, 279–296, <https://doi.org/10.1007/BF00119817>.
- Isabelle, P.-E., D. F. Nadeau, A. O. Perelet, E. R. Pardyjak, A. N. Rousseau, and F. Anctil, 2020: Application and evaluation of a two-wavelength scintillometry system for operation in a complex shallow boreal-forested valley. *Bound.-Layer Meteorol.*, **174**, 341–370, <https://doi.org/10.1007/s10546-019-00488-7>.
- Kohsiek, W., and M. Herben, 1983: Evaporation derived from optical and radio-wave scintillation. *Appl. Opt.*, **22**, 2566–2570, <https://doi.org/10.1364/AO.22.002566>.
- Kolmogorov, A. N., 1941: The local structure of turbulence in incompressible viscous fluid for very large Reynolds numbers. *C. R. Acad. Sci. URSS*, **30**, 301–305.
- Kooijmans, L. M., and O. K. Hartogensis, 2016: Surface-layer similarity functions for dissipation rate and structure parameters of temperature and humidity based on eleven field experiments. *Bound.-Layer Meteorol.*, **160**, 501–527, <https://doi.org/10.1007/s10546-016-0152-y>.
- Lagouarde, J.-P., J.-M. Bonnefond, Y. Kerr, K. McAneney, and M. Irvine, 2002: Integrated sensible heat flux measurements of a two-surface composite landscape using scintillometry. *Bound.-Layer Meteorol.*, **105**, 5–35, <https://doi.org/10.1023/A:1019631428921>.
- Leclerc, M. Y., and T. Foken, 2014: *Footprints in Micrometeorology and Ecology*. Springer, 258 pp.
- Li, D., E. Bou-Zeid, and H. A. De Bruin, 2012: Monin-Obukhov similarity functions for the structure parameters of temperature and humidity. *Bound.-Layer Meteorol.*, **145**, 45–67, <https://doi.org/10.1007/s10546-011-9660-y>.
- Lobos-Roco, F., O. Hartogensis, J. Vilà-Guerau de Arellano, A. de la Fuente, R. Muñoz, J. Rutllant, and F. Suárez, 2021: Local evaporation controlled by regional atmospheric circulation in the Altiplano of the Atacama Desert. *Atmos. Chem. Phys.*, **21**, 9125–9150, <https://doi.org/10.5194/acp-21-9125-2021>.
- Lüdi, A., F. Beyrich, and C. Matzler, 2005: Determination of the turbulent temperature–humidity correlation from scintillometric measurements. *Bound.-Layer Meteorol.*, **117**, 525–550, <https://doi.org/10.1007/s10546-005-1751-1>.

- Mahrt, L., D. Vickers, J. Sun, N. O. Jensen, H. Jørgensen, E. Par-dyjak, and H. Fernando, 2001: Determination of the surface drag coefficient. *Bound.-Layer Meteor.*, **99**, 249–276, <https://doi.org/10.1023/A:1018915228170>.
- Massman, W., 2000: A simple method for estimating frequency response corrections for eddy covariance systems. *Agric. For. Meteorol.*, **104**, 185–198, [https://doi.org/10.1016/S0168-1923\(00\)00164-7](https://doi.org/10.1016/S0168-1923(00)00164-7).
- Meijninger, W., O. Hartogensis, W. Kohsiek, J. Hoedjes, R. Zuurbier, and H. De Bruin, 2002: Determination of area-averaged sensible heat fluxes with a large aperture scintillometer over a heterogeneous surface—Flevoland field experiment. *Bound.-Layer Meteorol.*, **105**, 37–62, <https://doi.org/10.1023/A:1019647732027>.
- Meijninger, W. M. L., F. Beyrich, A. Ludi, W. Kohsiek, and H. D. Bruin, 2006: Scintillometer-based turbulent fluxes of sensible and latent heat over a heterogeneous land surface—A contribution to LITFASS-2003. *Bound.-Layer Meteorol.*, **121**, 89–110, <https://doi.org/10.1007/s10546-005-9022-8>.
- Monin, A. S., and A. M. Obukhov, 1954: Basic laws of turbulent mixing in the surface layer of the atmosphere. *Tr. Geofiz. Inst., Akad. Nauk SSSR*, **24**, 163–187.
- Munoz, R. C., M. J. Falvey, M. Arancibia, V. I. Astudillo, J. Elgueta, M. Ibarra, C. Santana, and C. Vasquez, 2018: Wind energy exploration over the Atacama Desert: A numerical model-guided observational program. *Bull. Amer. Meteor. Soc.*, **99**, 2079–2092, <https://doi.org/10.1175/BAMS-D-17-0019.1>.
- Neftel, A., C. Spirig, and C. Ammann, 2008: Application and test of a simple tool for operational footprint evaluations. *Environ. Pollut.*, **152**, 644–652, <https://doi.org/10.1016/j.envpol.2007.06.062>.
- Nordbo, A., S. Launiainen, I. Mammarella, M. Lepparanta, J. Huotari, A. Ojala, and T. Vesala, 2011: Long-term energy flux measurements and energy balance over a small boreal lake using eddy covariance technique. *J. Geophys. Res.*, **116**, D02119, <https://doi.org/10.1029/2010JD014542>.
- Oroud, I., 1999: Temperature and evaporation dynamics of saline solutions. *J. Hydrol.*, **226**, 1–10, [https://doi.org/10.1016/S0022-1694\(99\)00138-9](https://doi.org/10.1016/S0022-1694(99)00138-9).
- Rosen, M. R., 1994: The importance of groundwater in playas: A review of playa classifications and the sedimentology and hydrology of playas. *Paleoclimate and Basin Evolution of Playa Systems*, GSA Special Papers, Vol. 289, Geological Society of America, <https://doi.org/10.1130/SPE289-p1>.
- Rutllant, J. A., H. Fuenzalida, and P. Aceituno, 2003: Climate dynamics along the arid northern coast of Chile: The 1997–1998 Dinaica del Clima de la region de Antofagasta (DICLIMA) experiment. *J. Geophys. Res.*, **108**, 4538, <https://doi.org/10.1029/2002JD003357>.
- Salhotra, A. M., E. E. Adams, and D. R. Harleman, 1985: Effect of salinity and ionic composition on evaporation: Analysis of Dead Sea evaporation pans. *Water Resour. Res.*, **21**, 1336–1344, <https://doi.org/10.1029/WR021i009p01336>.
- Schuepp, P., M. Leclerc, J. MacPherson, and R. Desjardins, 1990: Footprint prediction of scalar fluxes from analytical solutions of the diffusion equation. *Bound.-Layer Meteorol.*, **50**, 355–373, <https://doi.org/10.1007/BF00120530>.
- Shuttleworth, W. J., 2008: Evapotranspiration measurement methods. *Southwest Hydrol.*, **7**, 22–23.
- Stoffer, R., 2018: Revisiting raw data processing of combined optical-microwave scintillometers. M.S. thesis, Wageningen University, 59 pp.
- Suarez, F., F. Lobos-Roco, A. De La Fuente, J. Vila-Guerau de Arellano, A. Prieto, C. Meruane, and O. Hartogensis, 2020: E-data: A comprehensive field campaign to investigate evaporation enhanced by advection in the hyper-arid Altiplano. *Water*, **12**, 745, <https://doi.org/10.3390/w12030745>.
- Tanny, J., S. Cohen, S. Assouline, F. Lange, A. Grava, D. Berger, B. Teltch, and M. Parlange, 2008: Evaporation from a small water reservoir: Direct measurements and estimates. *J. Hydrol.*, **351**, 218–229, <https://doi.org/10.1016/j.jhydrol.2007.12.012>.
- Tatarski, V. I., 1961: *Wave Propagation in a Turbulent Medium*. McGraw-Hill, 285 pp.
- Uribe, J., J. F. Munoz, J. Gironas, R. Oyarzun, E. Aguirre, and R. Aravena, 2015: Assessing groundwater recharge in an Andean closed basin using isotopic characterization and a rainfall runoff model: Salar del Huasco basin, Chile. *Hydrogeol. J.*, **23**, 1535–1551, <https://doi.org/10.1007/s10040-015-1300-z>.
- Vickers, D., and L. Mahrt, 1997: Quality control and flux sampling problems for tower and aircraft data. *J. Atmos. Oceanic Technol.*, **14**, 512–526, [https://doi.org/10.1175/1520-0426\(1997\)014<0512:QCAFSP>2.0.CO;2](https://doi.org/10.1175/1520-0426(1997)014<0512:QCAFSP>2.0.CO;2).
- Wang, T.-i., G. Ochs, and S. Clifford, 1978: A saturation-resistant optical scintillometer to measure CN₂. *J. Opt. Soc. Amer.*, **68**, 334–338, <https://doi.org/10.1364/JOSA.68.000334>.
- Ward, H., J. Evans, O. Hartogensis, A. Moene, H. De Bruin, and C. Grimmond, 2013: A critical revision of the estimation of the latent heat flux from two-wavelength scintillometry. *Quart. J. Roy. Meteor. Soc.*, **139**, 1912–1922, <https://doi.org/10.1002/qj.2076>.
- , J. G. Evans, C. S. B. Grimmond, and J. Bradford, 2015: Infrared and millimetre-wave scintillometry in the suburban environment—Part 1: Structure parameters. *Atmos. Meas. Tech.*, **8**, 1385–1405, <https://doi.org/10.5194/amt-8-1385-2015>.
- Wieringa, J., 1976: An objective exposure correction method for average wind speeds measured at a sheltered location. *Quart. J. Roy. Meteor. Soc.*, **102**, 241–253, <https://doi.org/10.1002/qj.49710243119>.
- Wilczack, J., S. Oncley, and S. Stage, 2001: Sonic anemometers tilt corrections algorithms. *Bound.-Layer Meteorol.*, **99**, 127–150, <https://doi.org/10.1023/A:1018966204465>.
- Wyngaard, J., Y. Izumi, and S. A. Collins, 1971: Behavior of the refractive-index-structure parameter near the ground. *J. Opt. Soc. Amer.*, **61**, 1646–1650, <https://doi.org/10.1364/JOSA.61.001646>.
- Zhang, G., J. Zhang, and P. Meng, 2021: Estimation of kilometer-scale heat fluxes over a hilly area in northern China using an optical-microwave scintillometer. *Agric. Water Manage.*, **244**, 106582, <https://doi.org/10.1016/j.agwat.2020.106582>.